A numerical study of fatigue of hardened cement paste at the microscale

Gan, Yidong; Zhang, Hongzhi; Liang, Minfei; Schlangen, Erik; van Breugel, Klaas; Šavija, Branko

Important note
To cite this publication, please use the final published version (if applicable).
Please check the document version above.

A numerical study of fatigue of hardened cement paste at the microscale

Yidong Gan [a],[*], Hongzhi Zhang [b], Minfei Liang [a], Erik Schlangen [a], Klaas van Breugel [a], Branko Šavija [a]

[a] *Microlab, Faculty of Civil Engineering and Geosciences, Delft University of Technology, Delft 2628, CN, the Netherlands*
[b] *School of Qilu Transportation, Shandong University, Jinan, PR China*

ABSTRACT

In this study, a numerical model using a 2D lattice network is developed to investigate the fatigue behaviour of cement paste at the microscale. Images of 2D microstructures of cement pastes obtained from XCT tests are used as inputs and mapped to the lattice model. Different local mechanical and fatigue properties are assigned to different phases of the cement paste. A cyclic constitutive law is proposed for considering the fatigue damage evolution. Fatigue experiments performed at the same length scale are used to calibrate and validate the model. The proposed model can reproduce well the flexural fatigue experimental results, in terms of *S-N* curve, stiffness degradation and residual deformation. The validated model is then used to predict the uniaxial tensile fatigue fracture of cement paste. The effects of microstructure and stress level on the fatigue fracture are studied using the proposed model. This model forms a basis for the multiscale analysis of concrete fatigue.

1. Introduction

Many concrete structures, such as off-shore structures and bridges, are subjected to fatigue loadings [1–3]. Fatigue results in progressive, permanent changes in the material, which are mostly formulated in terms of microcracks growth [4,5]. In general, the material deterioration induced by fatigue may cause structural failure and also undermine the durability of concrete structures [6,7]. Therefore, understanding of the fatigue behaviour of concrete is of significant practical importance and scientific interest.

Over the past few decades, many theoretical and numerical models have been proposed to study the fatigue of concrete, such as the empirical *S-N* method [1,2,8], fracture mechanics models based on the Paris' law and its modifications [9–14], fictitious crack models [15,16] and continuum damage mechanics models [17,18]. Most models focus on describing the macroscopic fatigue behaviour of concrete by fitting macroscopic experimental results, which can be applied directly to structural analysis. In general, in these models concrete is considered to be homogeneous. However, it is well known that concrete is a complex system with the multiscale heterogeneity ranging from nanometres to centimeters [19–21]. The phenomenon of concrete fatigue inherently involves multiple spatial scales. Nowadays, there is an increasing interest for multiscale modelling [22], which could connect the

heterogeneous material structures and properties at finer scales with the macroscopic behaviour of concrete. Several attempts have been made to investigate the effect of mesostructure of concrete on the global fatigue behaviour [23–25]. The content and shape of aggregate and the local fatigue properties of the paste matrix and the interfacial transition zone (ITZ) can be properly considered in these mesostructure-informed models. However, no model has been developed to date for fatigue of cement paste at the microscale. At this scale, the cement paste is mainly composed of calcium hydroxide (CH), unhydrated cement (UHC), calcium-silicate-hydrate (C-S-H) and pores of various sizes. For a complete and sophisticated multiscale modelling scheme, the model has to be established and validated at different subsequent scales. Therefore, the present study aims to develop and validate a microstructure-informed model to investigate the fatigue behaviour of cement paste at the microscale.

Since the presence of heterogeneities at different levels of observations complicates fatigue fracture, the first challenge is to choose an appropriate model to consider the heterogeneity. From the perspective of statistical physics, lattice type models have shown to be quite useful in dealing with the disorder in quasi-brittle materials [26]. Lattice models have been successfully used in simulating the fracture and deformation behaviours of cementitious materials [27–33]. In these models, the material is discretized into a network (i.e. lattice) of elements. Different properties of interest, e.g. mechanical and transport properties, could be

---

Nomenclature

A	cross-section area of the beam element
a, b	two parameters describing the fatigue properties
C_t	fitting parameter
D	fatigue damage index
D_i	fatigue damage index at the i-th analysis step
d_{soft}	constant percentage of reduction in strength
E_n	elastic modulus of the element
E_{d1}	fatigue damaged elastic modulus
f_t	tensile strength of the element
f_a, f_b	remaining strength of the element
f_{HZ}	loading frequency
J_{tot}	total material compliance under cyclic loading
$J(t,t_0)$	basic creep compliance
ΔJ_f	fatigue compliance due to the crack growth
M	local bending moment of the element
N	local normal force of the element
N_i	fatigue life of element at the i-th analysis step

S_i	stress level of the element at the i-th analysis step
t	fatigue loading time
t_0	beginning time
t_1	time unit
W	cross-sectional moment of resistance
α_N	normal force influence factor
α_M	bending influence factor
α_c, β_c	two creep parameters
ε_0	strain at the peak stress
$\varepsilon_a, \varepsilon_b$	strain at the remaining strength
ε_c	constant compressive strain
$\varepsilon_{p1}, \varepsilon_{p2}$	residual strain of the element
ε_{max}	maximum strain
$\Delta\sigma$	fatigue stress amplitude
σ_c	comparative stress
$\sigma_{sf}, \varepsilon_f$	highest comparative stress and corresponding residual strain
γ	constant exponent

assigned to these [32,34,35]. The material heterogeneity at various levels of observations can be directly implemented into the model by adjusting the local properties of lattice elements [36,37]. When the fracture of cement-based material under monotonic loading is examined, the cracks simulated by the lattice fracture are very realistic and resemble to the experimentally observed cracks [22,38,39]. In the current study, the lattice fracture model is further extended to mimic the fatigue fracture process by considering the local fatigue properties.

The paper is organized as follows: the fatigue lattice model is first established by considering the microstructure of cement paste and local fatigue damage evolution. Microscale flexural fatigue test results from the authors' recent work [40] are used to directly calibrate and validate the model. Then uniaxial tensile fatigue simulations are performed to investigate the effects of microstructure and stress level on the global fatigue fracture behaviour. The fatigue simulations are also compared with static simulations to gain more insights in the fatigue fracture process.

2. Numerical approach

2.1. Experimentally-obtained 2D virtual specimens

In general, the heterogenous microstructure of cement paste can be obtained by either experimental methods, e.g. scanning electron microscopy (SEM) [25] and X-ray computed microtomography (XCT) [31,36], or computer-generated approaches, e.g. HYMOSTRUC [41], μic [42] and CEMHYD3D [43]. In this study, miniatured cement paste specimens are fabricated and scanned by XCT to obtain the realistic microstructure. Standard grade CEM I 42.5 N Portland cement is mixed with deionized water to prepare the cement paste. Two water-to-cement (w/c) ratios, i.e. 0.4 and 0.5, are used. After sealed curing for 28 days, the cement paste is cut by a precision micro-dicing machine (MicroAce Series 3 Dicing Saw) to generate micro-cantilever beams with a square cross section of $300 \times 300 \ \mu m^2$. The cantilevered length of the beam is around 1650 μm. For more experimental details regarding the preparation process of micro-cantilever beams (MCB), the reader is referred to previous work of the authors [44,45].

Three beams for each w/c ratio are then scanned using XCT to obtain greyscale-based 2D images, see Fig. 1(a). The X-ray source tube is set at 90 kV/100 μA during scanning, which results in a voxel resolution of 0.5

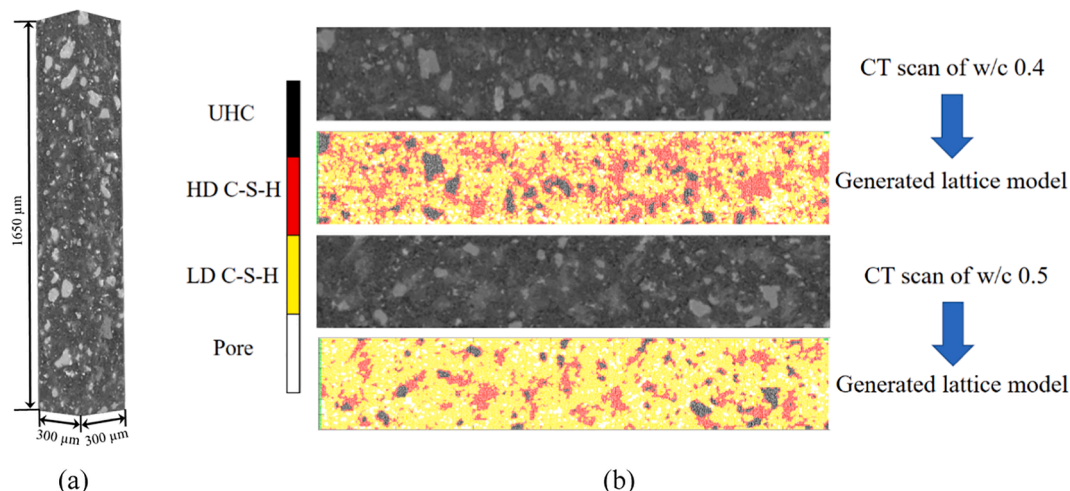**Fig. 1.** (a) The CT image of a micro-cantilever beam; (b) segmentation results for different w/c ratios.

$\times$ 0.5 $\times$ 0.5 μm³. The segmentation procedure using the global thresholding method [33,46] is performed on these CT images. Three threshold values are defined to segment different components in the cement paste based on the grey-scale histogram. These threshold values are determined by using either the inflection point of the cumulative grey-scale value curve or the change of the tangent slope [33,46].

The hydration degree and w/c ratio are also used as inputs to segment the main hydration products [47]. As is shown in Fig. 1(b), four main phases, i.e. unhydrated cement (UHC), high-density (HD) C-S-H, low-density (LD) C-S-H and pores, can be distinguished after the segmentation. It should be mentioned that other hydration products, e.g. calcium hydroxide (CH), ettringite (AFt) and monosulfate (AFm), are not segmented in this study and consequently they are embedded in other segmented phases. More details on the segmentation procedure can be found in [33,35,46]. Before the construction of the lattice network, the spatial resolution of XCT images is reduced to 5 μm/pixel using the bilinear interpolation algorithm to save computational time. Note that, if a different resolution would be used in the model, the calibration process should be repeated.

2.2. General description of lattice model

2.2.1. Domain discretization

The first step of lattice model construction is to discretize the material structure by a lattice network. A group of cells is generated based on the pixel images obtained from XCT tests, and each cell coincides with a single pixel. In each pixel, a sub-cell is created and the length ratio of the sub-cell to the cell, which is defined as the randomness, is set to be 0.5 here [48]. Subsequently, a node is randomly created inside each sub-cell by using a pseudo-random number generator. Delaunay triangulation of the domain is then performed on these nodes as is described in [34,49,50]. The neighboring nodes are connected to form the lattice network, see Fig. 2. The reason for using irregular lattice networks is to introduce local heterogeneity and disorder and avoid mesh dependence of crack paths [27]. By assigning these beams with different properties, the microstructure of the material can be mapped on the lattice network. Fig. 1(b) shows the generated lattice models for two w/c ratios based on the segmented 2D virtual specimens, which are 2D slices randomly selected from the 3D CT-scanned specimen.

2.2.2. Mechanical constitutive law

In the lattice model, the cement paste is discretized as a set of Timoshenko beam elements. All beam elements are assumed to exhibit linear elastic brittle behaviour with different elastic modulus and maximum strength, depending on the XCT images. Under pre-defined boundary conditions, a linear elastic analysis is performed and the node displacement of each element is calculated. Details about the numerical algorithms can be found in [33,50,51]. To simulate the fracture process, removing (or par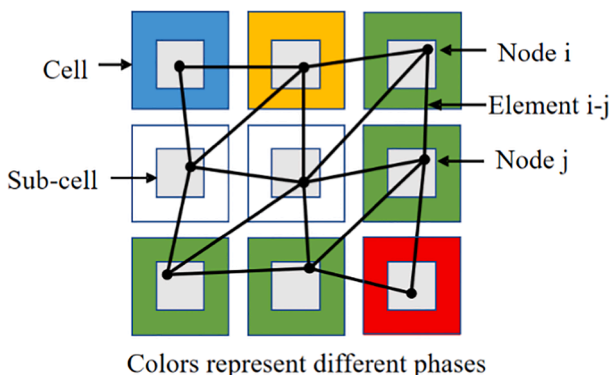tially removing) of lattice beams is done step-by-step upon reaching a certain criterion [27,30]. For the determination of fracture criterion in the case of monotonic loading, the comparative stress σ_c is calculated by the combination of normal force and bending moment [27], as follows:

$$\sigma_c = \alpha_N \frac{N}{A} + \alpha_M \frac{M}{W} \tag{1}$$

where A denotes the cross-section area of the beam element; W is the cross-sectional moment of resistance; N and M are the local normal force and bending moment, respectively. α_N and α_M represent the normal force influence factor and the bending influence factor, which are generally chosen as 1.0 and 0.05, respectively [48,50,52]. The effect of these factors on the overall fracture behaviour is discussed elsewhere [53]. The stress level in each element is calculated by dividing the comparative stress with the defined local tensile strength f_t of the element. The critical element, which has the highest stress level, is then partly removed from the system following the same softening cyclic constitutive law described in Section 2.3.1 to represent the cracking. The local elastic moduli E_n and tensile strengths f_t of different phases, obtained in our previous work [33], are summarized in Table 1. The strain at the peak stress ε_0 for each phase is also given.

Note that, for the interface elements between two different phases, the lower mechanical properties among these two phases are assigned [33]. For experiments, after the preparations of micro-cantilever beams (MCB), a KLA Nano indenter G200 is used to conduct bending tests on these MCBs [44,45]. The baseplate of beams is first attached on a flat metal surface using cyanoacrylate adhesive. A cylindrical wedge indenter tip with a length of 200 μm is used to apply vertical line loads at the free end of the beams. In the simulations, the same boundary condition with the experiments is applied on virtual samples, as is illustrated in Fig. 3(a): the static load is imposed on one side of the virtual sample and the other end of the sample is fixed. A typical simulated stress–strain curve as well as the fracture pattern for a flexural static test is shown in Fig. 3. Generally, the major crack will initiate at the weakest locations near the fixed end and propagates into the beam leading to complete fracture. The red zig-zag lines observed in the post-peak response can be explained by the fact that after a beam element is removed, much less load is required to break the next beam in the system, after which again a higher load is needed to continue further. This behaviour demonstrates the local instabilities during the crack formation and propagation in quasi-brittle materials. The local mechanical properties will serve as the initial properties in the following fatigue simulations.

2.3. Fatigue lattice model

2.3.1. Cyclic constitutive law

When the model is subjected to the cyclic stress with the magnitude lower than the macroscopic strength, the lattice system will never fail. Therefore, a cyclic constitutive law incorporating the fatigue damage evolution is used here to consider the degradation of mechanical properties under fatigue loading. In reality, the fatigue damage of cementitious material mainly consists of the progressive growth of internal microcracks [6,54]. The growth of a microcrack manifests itself through degradation of macroscopic properties, such as stiffness. To account for this behaviour, the cyclic constitutive law for a lattice beam element is proposed, as is shown in Fig. 4. The cyclic stress-strain curve for describing the mesoscopic fatigue behaviour is originally developed by

Fig. 2. Lattice element generation procedure.

Table 1
Local properties for different phases in hydrated cement paste [33].

Phases	f_t (MPa)	E_n (GPa)	ε_0 (με)
UHC	614.7	84.2	7300
LD C-S-H	52.2	21.3	2451
HD C-S-H	82.8	26.4	3136
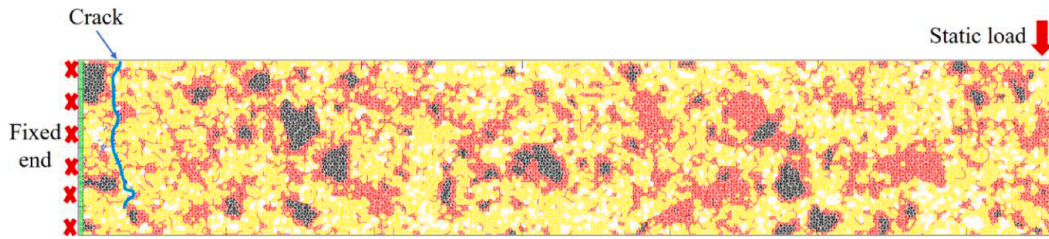
(a)
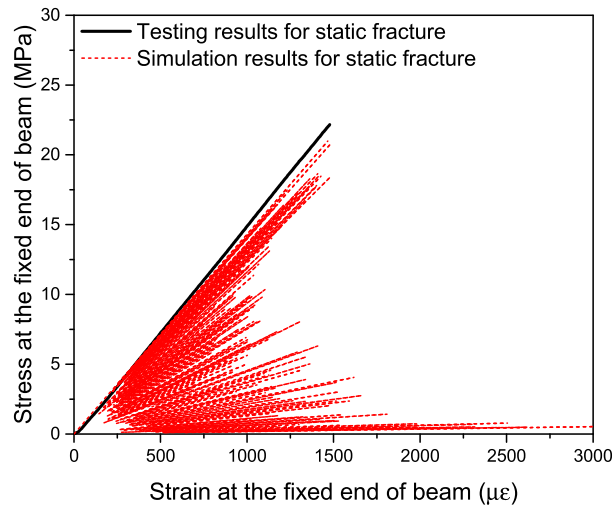
(b)

Fig. 3. Simulation results of one w/c 0.4 sample (1650 μm × 300 μm). (a) The fracture pattern under static loading; (b) the comparison of the stress–strain curve with experimental results.
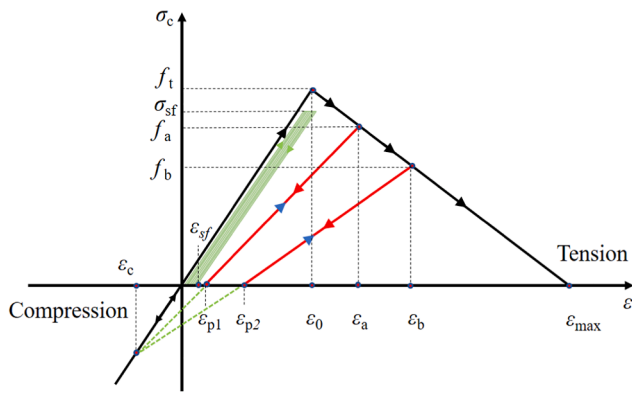

Fig. 4. The constitutive law of individual lattice elements subjected to cyclic loading.

Nagai et al. [55], and further modified by Gong et al. [23]. This cyclic law is similar to the continuous-function model developed by Hordijk [15] for simulating the post-peak cyclic behaviour of the crack in concrete.

At each analysis step of the fatigue fracture simulation, the maximum fatigue load is imposed on the system. The comparative stress and corresponding stress level in every lattice element are calculated. Based on the stress levels and the number of cycles, the calculated fatigue damage in the form of mechanical degradation is then assigned into all damaged beams. For the unloading stage, it is assumed that the unloading process will not generate any damage such that the reloading curve (blue arrow) will overlap with the previous unloading curve (red arrow). Moreover,

based on the experimental fact [23,40,45], there are always residual strains under cyclic loading. Therefore, the unloading curve in each loading cycle will not pass through the origin, see Fig. 4. More details regarding the determination of residual strain will be discussed in Section 2.3.2. After unloading, the system will be updated due to the new stiffness matrix and the remaining strength of each element. If the global stiffness of the system falls below 20% of its original stiffness, the simulation is stopped and the system is considered to have failed. Otherwise, another analysis step is executed. Note that an analysis step does not always represent one loading cycle as is explained in next paragraph.

As is shown in Fig. 4, the beam is assumed to be purely linear elastic when in compression and neither compressive failure or compressive fatigue damage will not occur. Only the mechanical properties of beams that are subjected to comparative tensile stress will gradually decrease depending on the stress level and number of cycles. When in tensile, the pre-peak regime is characterized by the initial strength f_t and elastic modulus (f_t/ε_0) of the beam element, which are identical to the static mechanical properties (Table 1).

There are two scenarios for the implementation of fatigue damage at the microscale. Firstly, if the calculated highest comparative stress is lower than its remaining strength (i.e. $\sigma_{sf} < f_t$), the mechanical properties of all the beams will be reduced based on the current stress level (green lines in Fig. 4). Each phase in cement paste is assigned with a fatigue property following the phenomenological *S-N* approach [1,3], which reads as:

$$S_i = a \cdot \log(N_i) + b \tag{2}$$

where S_i is the stress level of the element at the *i*-th analysis step; N_i is the corresponding fatigue life; *a* and *b* are two major parameters deciding

the fatigue properties of hydrated cement paste phases. In this study, the parameters a and b for different phases, namely LD C-S-H and HD C-S-H, will be determined by fitting the simulation results to experimental results. Based on Eq. (2), the fatigue life can be calculated if the stress level is known, and vice versa.

Another important parameter is the fatigue damage index D, defined as the reduction percentage of strength with respect to the initial strength of the element. Therefore, the remaining strength of the damaged element is calculated as $(1 - D)f_t$. When $D = 0$ the element is assumed to be undamaged, and when $D = 1$ the element will be removed from the mesh. Note that the same fatigue damage index is used for the elastic modulus of a damaged element in the current scenario. Generally, the fatigue damage D for each element should be accumulated with increasing number of cycles, and a higher stress level results in a higher degree of fatigue damage. Since the stiffness matrix is always updated due to the fatigue damage, the stress in the element will be redistributed in each loading cycle. Therefore, in order to consider the effect of redistribution of stress during the cyclic loading, the fatigue damage D_i at the i-th step is calculated based on the Miner's rule [56] and the fatigue damage at previous step D_{i-1}:

$$D_i = \frac{n_c}{N_i} + D_{i-1} \tag{3}$$

where n_c is defined as the cycle block for each analysis step and N_i is the fatigue life calculated from Eq. (2) based on the i-th step of stress level. It should be mentioned that, even though the Miner's law may not precisely reflect the actual fatigue damage evolution of cementitious material and may lead to unconservative results, this law is widely used for its simplicity [15,57–59]. An alternative would be to consider the fatigue damage evolution using thermodynamic concepts under the damage mechanics framework, as was proposed in [4,60].

In general, a high-cycle fatigue test of cement paste under a moderate stress level involves tens of thousands of cycles. It is inefficient to explicitly simulate every loading cycle. Therefore, a proper accelerated strategy is preferred for fatigue damage simulation. To this end, the "block cycle jump" technique, in which a certain number of cycles are packaged as one block loading case, is usually adopted [61]. Similarly, an appropriate amount of cycles is chosen as the cycle block defined in Eq. (3) to speed up the fatigue simulation in this study. The effect of cycle block value on the simulated fatigue life and computational time is shown in Fig. 5. It can be seen that the increasing value of cycle block from 10 to 1000 leads to a slightly higher fatigue life. However, the computational time is reduced significantly due to the increasing cycle block. In this study, a pre-defined value of 1000 is used for the cycle block. This means that the fatigue damage for 1000 cycles can be
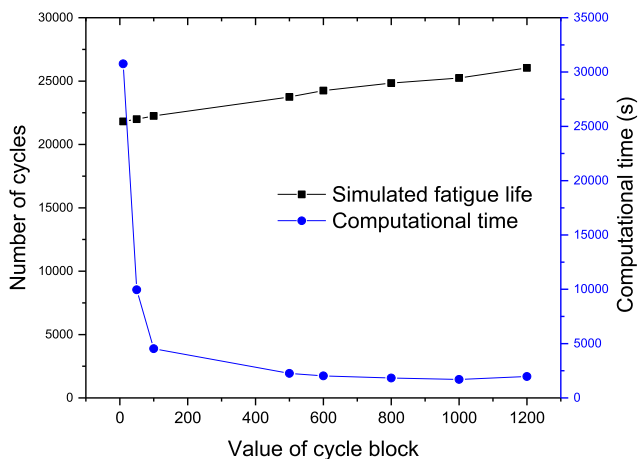

Fig. 5. The effect of cycle block value on the simulated fatigue life and computational time.

considered in one analysis step. It should also be noted that, if the cycle block value is very close to or even higher than the final fatigue life, the simulation may generate unrealistic results. Therefore, the value of cycle block will be adjusted for each simulation until it is at least ten times lower than the final fatigue life.

The second case for considering the fatigue damage is that when the calculated highest stress level for the critical element exceeds 1 (i.e. $\sigma_{sf}/f_t > 1$): a post-peak cyclic softening behaviour is assumed for this element, see Fig. 4. In this case, the remaining strength of the element is gradually reduced following a linear softening curve [15,55,62]. For simplicity, only four softening steps are required for an element to reach the final fracture. At each softening step, a certain percentage of reduction d_{soft} in strength is assumed for this element, e.g. $f_a = (1 - d_{soft})f_t$ and $f_b = (1 - d_{soft})^2 f_t$. Therefore, the fatigue damage index of this element at the i-th step should be $D_i = 1 - (1 - d_{soft})(1 - D_{i-1})$. Following the approach described in [23], a constant strain ($\varepsilon_c = -400$ με) at the compression branch is introduced for all phases to determine the reduction percentage of elastic moduli and the residual strains (e.g. ε_{p1} and ε_{p2}). When the maximum strain ε_{max} is also known, the residual strain ε_{p1} and the corresponding damaged elastic modulus E_{d1} of the element can be calculated using the following equations:

$$\varepsilon_{p1} = \frac{d_{soft}\varepsilon_c(\varepsilon_0 - \varepsilon_{max})}{\varepsilon_0 - \varepsilon_c} \tag{4}$$

$$E_{d1} = \frac{(1 - D_i)f_t}{\varepsilon_a - \varepsilon_{p1}} \tag{5}$$

Note that the UHC phase is assumed to have infinite fatigue life without any fatigue damage accumulation. Only two C-S-H phases in the cement paste are assumed to experience fatigue damage. The calibration of parameters for characterizing the fatigue damage evolution and residual deformation will be performed in Section 3.

2.3.2. Residual deformation

Another important characteristic of fatigue test is the residual deformation. It has been suggested that the residual deformation is mainly attributed to the creep deformation and fatigue crack growth [1,11]. For each analysis step in the fatigue simulation, the local residual deformation of each element will be determined and then imposed on the lattice elements to calculate the macroscopic residual deformation through the approach described in [33]. In this study, the change of strain at the maximum fatigue load is defined as the residual strain and the fatigue compliance is defined by dividing the residual strain by the half of the applied maximum stress.

For the case of $\sigma_{sf}/f_t > 1$, the residual deformation of the critical element is determined based on the post-peak cyclic behaviour as is depicted in Fig. 4. If the stresses in all elements are lower than their strengths, the residual deformation of each element will be calculated considering the creep and fatigue crack growth. In this case the cycle block is also used to accelerate the fatigue analysis in one analysis step. Bažant and Hubler [23] developed a theoretical model to relate the macroscopic deformation of concrete with the microscopic fatigue crack growth based on the Paris law. According to [23], the total material compliance J_{tot} under cyclic loading is:

$$J_{tot} = J(t, t_0) + \Delta J_f \tag{6}$$

$$J(t, t_0) = \alpha_c \left(\frac{t - t_0}{t_1}\right)^{\beta_c} \tag{7}$$

$$\Delta J_f = C_t \cdot t \cdot f_{Hz} \left(\frac{\Delta\sigma}{f_t}\right)^{\gamma} \tag{8}$$

where $J(t,t_0)$ is the basic creep compliance given in [44,63]. It is defined as the creep strain at time t caused by a unit stress applied at the beginning time t_0. t_1 is the time unit. α_c and β_c are two creep parameters of each phase and ΔJ_f is fatigue compliance due to the crack growth

under cyclic loading [23]. The exponent γ is a constant with the value of 4 [11,23] and C_t is a fitting parameter [23]. $\Delta\sigma$ is the fatigue stress amplitude of the element and f_{HZ} is the loading frequency. The time needed for one complete cycle equals to the inverse of loading frequency, i.e. $1/f_{HZ}$. Therefore, the number of cycles N can be calculated as $t \cdot f_{HZ}$. Note that the current model is only applicable for the fatigue loading with a low loading frequency. When the higher loading frequency is used, the inertia effect of fatigue loading begins to play a role and should be taken into account [64,65].

3. Model calibration and validation

The flexural fatigue tests on the MCBs are performed and the Reader is referred to [40] for details. The experimental results in terms of S-N curves, stiffness degradations and residual deformation evolutions of MCBs have been used to calibrate the 2D flexural fatigue lattice model. As there is almost no other available experimental data for the cement paste at the microscale in literature, the validation is carried out by simulating samples that have not been used in the calibration phase. These samples differ in microstructures and w/c ratios. In the validation phase, parameter adjustment is not permitted. The calibration is first conducted on the sample with the w/c of 0.4 and the calibrated parameters for two C-S-H phases are summarized in Table 2.

For the calibration of parameters determining the fatigue compliance evolution at the free end of the beam, the same loading protocols as the experiments described in [40], in terms of loading frequency (0.55 Hz), number of cycles (5 0 0) and stress level (80%), are used in the simulation. The value cycle block is chosen as 1 for this case. It means that each of the 500 cycles is explicitly simulated. The creep parameters for two C-S-H phases are calibrated using the recently obtained basic creep compliance results [66]. From a trial-and-error method, the parameters responsible for the fatigue crack growth are obtained (Table 2). Since it is currently impossible to measure the maximum strain of each phase at this scale, both C-S-H phases are simply assumed to have the same maximum strain ε_{max} (3200 $\mu\varepsilon$) slightly larger than the strain at the peak stress ε_0 (3136 $\mu\varepsilon$). In Fig. 6, the fatigue compliance developments of different virtual samples are compared with the experimentally measured fatigue compliance (average values with standard deviations). The figure shows that most of the simulated fatigue compliance curves using calibrated parameters lie in the range of the experimental results. Large scatter still exists in the magnitudes of simulated fatigue compliance for different virtual samples mainly due to the heterogeneous microstructures, which is also observed in experiments [40].

Meanwhile, the parameters for describing the fatigue damage evolution have been calibrated using experimentally obtained S-N relationships. Firstly, the effect of the fatigue parameter b on the simulated S-N curve is investigated and shown in Fig. 7. In general, the global fatigue life increases with increasing the value of b. To simplify the calibration process, the b is chosen as 1.1 for both C-S-H phases.

Before the determination of the fatigue parameter a, several pairs of values for the two phases, i.e. LD C-S-H and HD C-S-H, have been used for trial simulations. The simulated S-N curves for one virtual specimen (w/c 0.4) using different fatigue parameters are compared with experimental results [40] and shown in Fig. 8. At a given stress level, the global fatigue life decreases with the increasing magnitudes of fatigue parameters (or decreasing of local fatigue properties). Moreover, for w/c
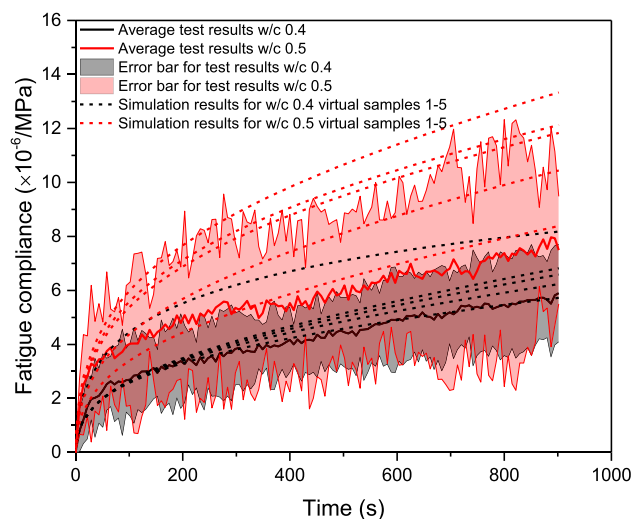

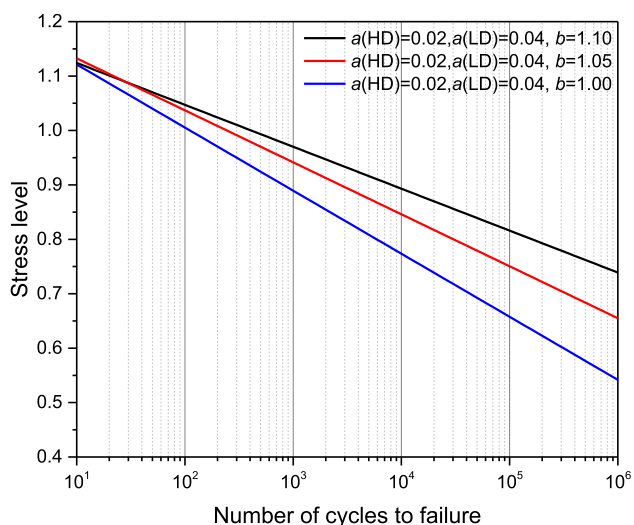**Fig. 6.** The comparison of experimentally measured fatigue compliances and simulation results.

Fig. 7. The effect of b on the simulated S-N curves.

0.4 sample, the fatigue parameter of LD C-S-H seems to be more influential than that of HD C-S-H with respect to the fatigue life. For the virtual sample used in the simulation, the two parameters with the values $a(HD) = 0.02$ and $a(LD) = 0.04$ seem to fit well with the experimental results. Therefore, these two values are adopted in the simulations for other w/c 0.4 virtual samples and w/c 0.5 virtual samples with different microstructures. For each virtual sample, three different stress levels are applied. The simulated S-N curves are compared with experimental results and shown in Fig. 9. A wide variation of simulated fatigue life for different virtual samples can be observed in Fig. 9. However, it should be pointed out that each virtual sample follows a unique linear S-N curve on the semi-log scale. It indicates that the major source of scatter in the result of fatigue simulation originates from the heterogeneous material microstructure. It is worth noting that another source of uncertainty for fatigue results comes from the determination of the true static strength, which is used to determine the nominal stress level. This problem can also be tackled in the simulations. Despite the large variation between individual samples, it has been clearly demonstrated that there is a significant difference in fatigue life for two w/c ratios, see Fig. 9.

Two examples of simulated fatigue fracture patterns are shown in

Table 2
Calibrated parameters for the fatigue simulation.

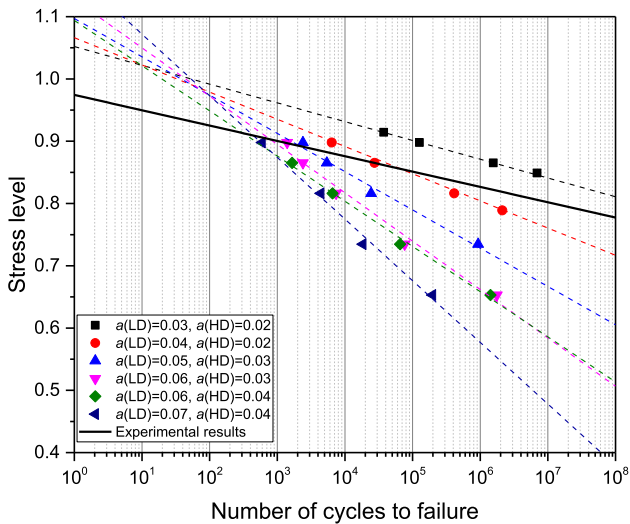| Phases	a	b	α_c (10^{-6}/ MPa)	β_c	C_t (10^{-6}/ MPa)	ε_{max} ($\mu\varepsilon$)	d_{soft} (%)
HD C-S-H	0.02	1.1	0.23	0.20	5×10^{-6}	3200	20
LD C-S-H	0.04	1.1	0.34	0.20	1.2×10^{-5}	3200	20

Fig. 8. Simulated S-N curves for one virtual sample using different fatigue parameters.
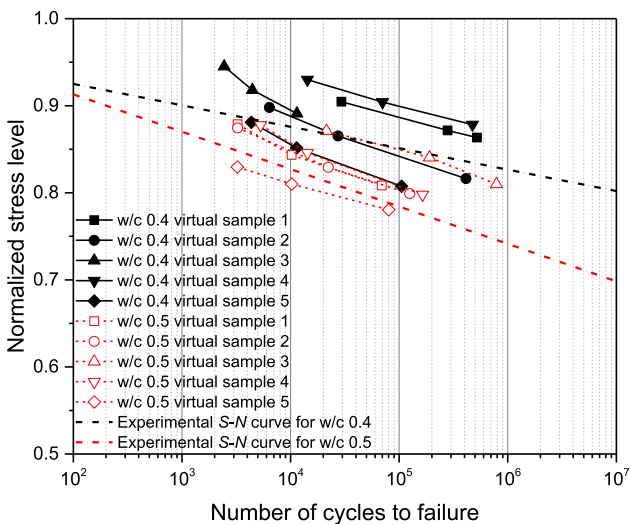

Fig. 9. The simulated S-N curves for different virtual samples.

Fig. 10. Interestingly, multiple cracks have been observed for some fatigue flexural simulations, see the w/c 0.4 virtual sample in Fig. 10. Similar findings have been found in experimental results reported in literature [10,12,67,68]: more diffuse microcracks have been detected in the specimens in fatigue tests compared to the static fracture tests. Besides, the w/c 0.4 sample is actually more heterogeneous compared to the w/c 0.5 specimen. Therefore, the possibility for the multiple cracking could also be higher. In general, the crack initiates at the weakest locations, e.g. LD C-S-H phases, under both static and fatigue loadings. It is clear that the mechanical properties of each phase are important for the fatigue fracture behaviour. The major difference is that, when one propagating crack is impeded by other phases with higher fatigue resistances, i.e. HD C-S-H or UHC, this crack may branch or continue to propagate depending on the stress level, number of cycles as well as the accumulated fatigue damage in the surrounding phases. Since all C-S-H phases are simultaneously experiencing some degrees of fatigue damage in previous loading cycles and the fatigue damage evolution for HD C-S-H is much slower than that of LD C-S-H, some cracks may also initiate in LD C-S-H at other locations. Due to the updated global stiffness according to the fatigue damage accumulation, the stress redistribution will occur under each flexural cyclic loading and may lead to the presence of multiple cracks. However, it should be mentioned that this situation may only apply at the low stress level as the difference in fatigue life for two C-S-H phases is significant. When the stress in an element is slightly lower than the its strength, the fatigue life for two phases is very close and only differs by some cycles. This may indicate different fatigue fracture behaviours at different stress levels. If the stress level is high enough, the fatigue fracture tends to be identical with the static fracture behaviour. For instance, the fatigue fracture pattern of the w/c 0.5 virtual sample in Fig. 10 is similar to its static fracture. One can also envision that, by manipulating the difference of fatigue properties between the two C-S-H phases, the fatigue fracture pattern will be altered. Therefore, the quantification of the fatigue properties of two C-S-H phases is crucial for the fatigue fracture simulation of cement paste. In addition, the fatigue cracks in the simulations are dependent on the degree of heterogeneity and the distributions of different phases. This aspect will be further illustrated using the uniaxial tensile fatigue simulations in Section 4.

A typical stress-strain curve under the cyclic loading is presented in Fig. 11. With the increasing number of cycles, the slope of the loading cycle gradually decreases. To monitor the stress evolutions of beam elements under the flexural cyclic loading, the comparative stresses of beams at two locations, see Fig. 12 (a), have been extracted from the simulations. It can be seen that at the location 1, which is at the fixed end of beam, both stresses in LD C-S-H and HD C-S-H beams increase slowly
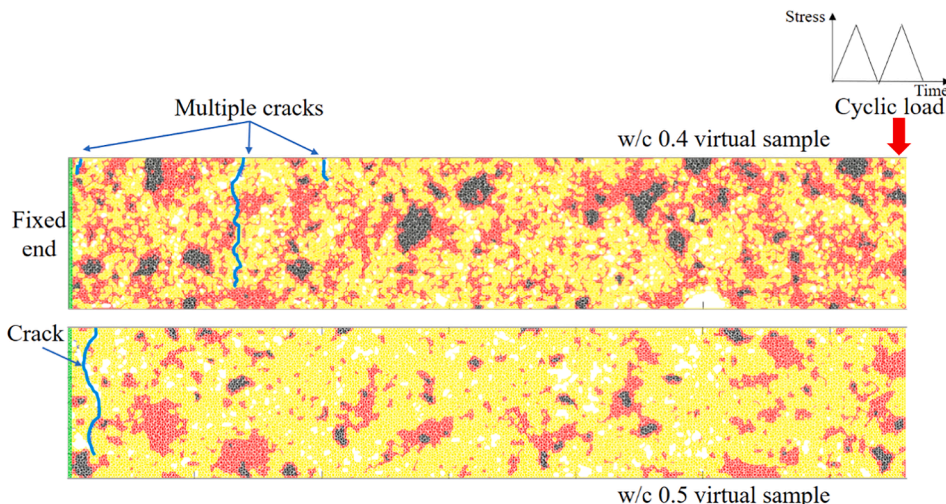

Fig. 10. Examples of the fatigue fracture patterns for w/c 0.4 and 0.5 virtual samples.
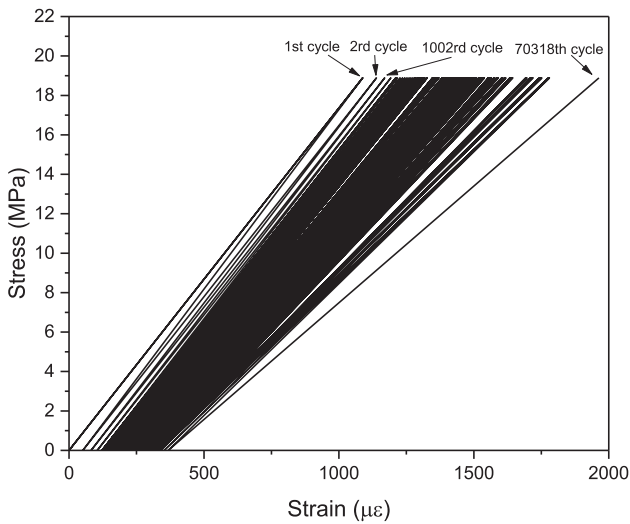
Fig. 11. A typical simulated stress-strain curve for one w/c 0.4 sample under cyclic loading with the upper stress level of 90%.

before the unstable cracking is reached. The UHC seems to remain constant during most of the fatigue life. On the contrary, the stresses of LD C-S-H and HD C-S-H beams at the location 2, which is at the vicinity of the major fatigue crack instead of the cracking tip, appear to gradually decrease with the increasing number of cycles. Similarly, the stresses in UHC elements remain almost constant before the unstable cracking. Note that the highest stress is always at the tip of the major crack due to the stress concentration. This would result in a higher degree of fatigue damage accumulated in these elements near the cracking tip. The beam elements at the location 2 is supposed to experience significant change of stress during the stress redistribution process, while the beam stresses

at the location 1 would show a gradual increase before the unstable cracking due to a relatively slower fatigue damage accumulation. It is also found that in both locations the stresses in UHC elements change much slower than those stresses in HD C-S-H and LD C-S-H beams, while the stresses in HD C-S-H also change slightly slower than those in LD C-S-H elements. This could be explained by less fatigue damage generated in these elements.

The changes of the global elastic moduli for virtual samples, which represent the stiffness degradations under fatigue loading, are shown in Fig. 13, along with the results of measurements. It can be seen that in most of the fatigue life the reduction of elastic modulus is very small. Overall, both the numerical and experimental results suggest a slow and limited flexural fatigue damage evolution process for cement paste at the microscale. Another important feature of fatigue fracture is that the fatigue crack becomes unstable when the total damage has accumulated to a certain degree. This is primarily because the remaining cross-section of the specimen can no longer sustain the external fatigue loading. It is manifested as a sudden drop of stiffness, as is shown in Fig. 13 (marked as blue lines).

4. 2D uniaxial tensile fatigue life and fracture behaviour

By using the calibrated lattice fatigue model, it is now possible to simulate the uniaxial tensile fatigue behaviour of cement paste at the microscale, which is difficult to investigate experimentally. The output of the uniaxial tensile fatigue simulations could also be used as input for the multiscale analysis of concrete [31,37]. The calibrated parameters from the previous section are adopted here to predict the uniaxial tensile fatigue life and fracture pattern of cement pastes. The microstructures of cement pastes (w/c 0.4) with the size of $500 \times 500 \ \mu m^2$ are extracted from the segmented CT results, see Fig. 14. In the uniaxial fatigue simulations, 8 virtual samples are generated, and each virtual sample is subjected to three different loading levels. Hence, in total 24 simulations
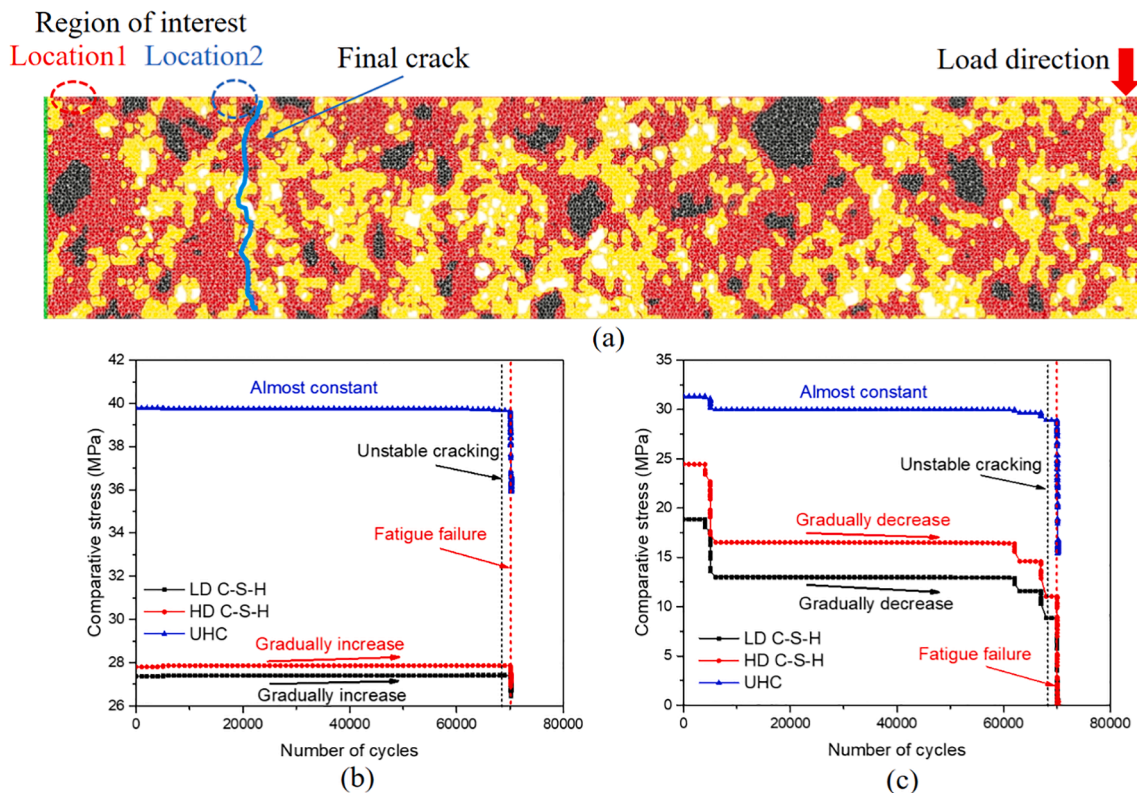

Fig. 12. The stress evolutions of different types of upper fiber beam elements in the region of interest under cyclic loading. (a) Fracture pattern; (b) location 1 and (c) location 2.
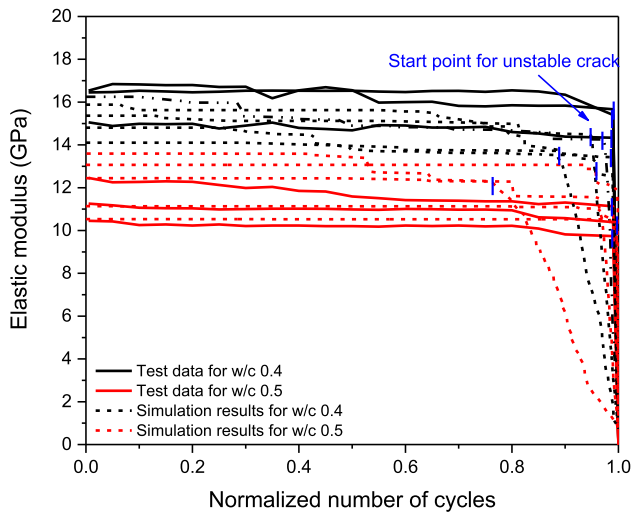
Fig. 13. The simulated elastic modulus degradation along with the experimental results.

are performed.

The simulated uniaxial tensile fatigue results for all virtual samples are summarized in Table 3. The obtained *S-N* curves of virtual samples and also the assumed local *S-N* curves for both C-S-H phases are shown in Fig. 15.

It is clear from both Table 3 and Fig. 15 that the fatigue life decreases with the increasing stress level. Similar to the flexural fatigue, each virtual sample subjected to uniaxial tensile fatigue also exhibits a unique *S-N* relationship and the difference in *S-N* curves between each sample is caused by the heterogeneous microstructures. Moreover, at a given stress level the uniaxial tensile fatigue life of cement paste is always lower than the pure C-S-H phases as is shown in Fig. 15. This is attributed to the presences of pores and stiff particles (UHC), which introduce stress concentrations into the system.

To gain more insights into the fatigue fracture behaviour, the fatigue cracks at different loading cycles are illustrated in Fig. 16. The loading cycles have been normalized to the final fatigue life. Note that the 3D features of fracture behaviour in heterogeneous materials cannot be reflected by the current 2D model. All analyses are performed based on 2D results. At the beginning of the fatigue simulations, the upper load of fatigue will sometimes generate a few initial cracks in the system, mostly distributed in LD C-S-H near the pores, see Fig. 16. Before the fatigue failure, the fatigue crack will always propagate following the weakest link in the system, which is similar to the static fracture behaviour.
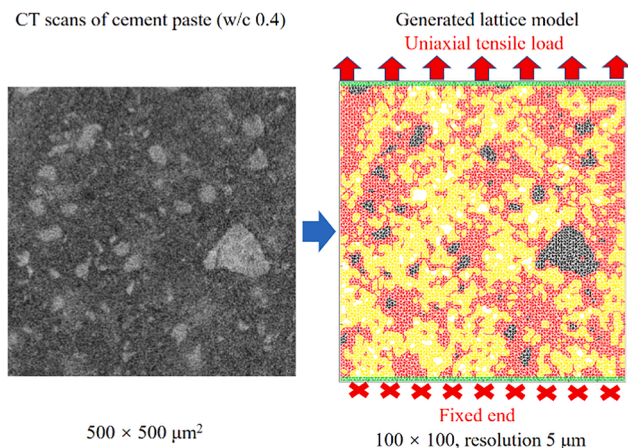

Fig. 14. The generated lattice model from CT scans for uniaxial tensile fatigue simulation.

Table 3
The simulation results for 8 virtual samples under uniaxial tensile fatigue.

| Virtual sample No.	Static tensile strength (MPa)	Stress level (%)	Fatigue life
1	16.01	82.45	532,462
		84.95	131,474
		87.42	37,470
2	16.10	86.97	237,598
		89.46	66,614
		91.94	22,574
3	10.84	81.17	462,306
		84.86	56,306
		88.55	9302
4	20.48	85.96	28,553
		87.92	11,553
		89.87	5553
5	17.79	85.43	104,534
		87.68	35,502
		89.93	13,518
6	18.45	84.55	238,509
		86.72	74,521
		88.88	27,501
7	17.56	86.54	191,526
		88.82	56,518
		91.09	17,526
8	19.18	85.53	40,522
		87.61	15,518
		91.78	3526
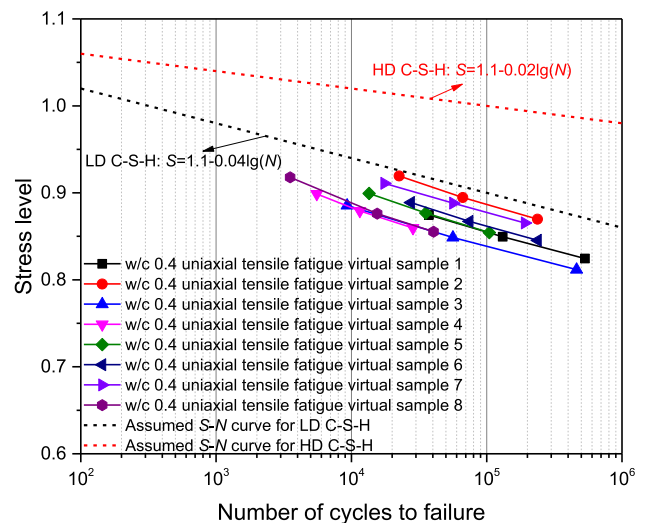
Fig. 15. Simulated uniaxial tensile fatigue *S-N* curves for w/c 0.4 virtual samples.

Therefore, for most simulations results the fatigue fracture patterns are similar to the static fracture patterns. For example, Fig. 16 shows that both the major static crack and fatigue crack pass through the disconnected pores and result in the final failure. This could also be attributed to the high stress levels used in these simulations, i.e. around 81–92% of static strength. However, it should be borne in mind that the fatigue fracture also depends on the local stress fields and fatigue damage evolution rates of different phases.

In order to demonstrate the different fatigue fracture behaviours at different stress levels using the developed fatigue lattice model, two stress levels, i.e. 85% and 50%, are applied on the same virtual sample. However, due to the high fatigue resistance of cement paste at the microscale, the simulated fatigue life at the low stress level (50%) will be at least 10^{14}–10^{15} cycles. Therefore, for the purpose of demonstration, lower fatigue properties are assigned to the two C-S-H phases, i.e. $\alpha(LD)$ = 0.09 and $\alpha(HD)$ = 0.04. It is worth mentioning that the situation using lower fatigue properties may be applicable for macroscopic fatigue simulation of concrete as the interface transition zone (ITZ) between the
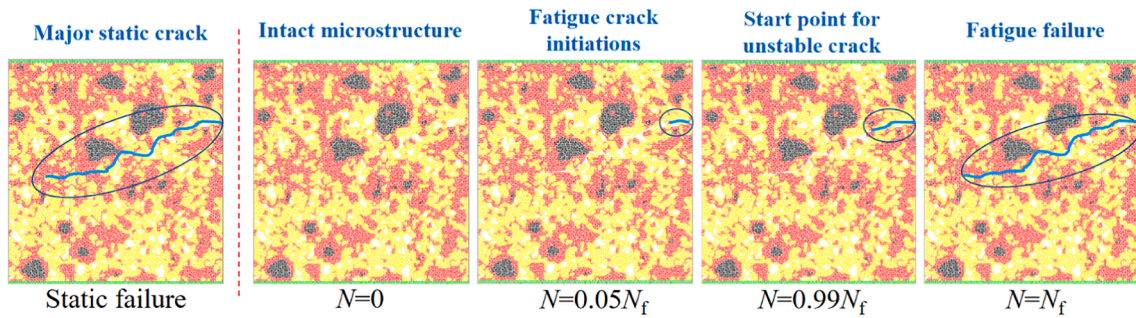
Fig. 16. One example of fatigue crack development in cement paste (w/c 0.4) under uniaxial tensile fatigue loading at the stress level of 87.4% and the simulated fatigue life N_f is 37470.

aggregate and cement paste is generally expected to have much lower fatigue resistance compared to the paste matrix [8,23,24,58,68–71]. The fatigue damage typically accumulates faster in these regions prompting the fatigue failure. The simulated fatigue patterns are shown in Fig. 17.

Fig. 17(a) shows that several cracks initiate at the early stage of fatigue loading (marked in blue circles) when the stress level is 85%. At this stress level, the local stresses near the crack tip are also high such that the rates of local fatigue damage evolution are at the same magnitude for both C-S-H phases, as have been explained before. As a result, the crack will propagate into both C-S-H phases alike. When the loading cycles reach the starting point for the unstable crack, this stage of cracking behaviour is similar to the static fracture. Therefore, the final fatigue crack resembles the static fracture in this high stress level. However, in Fig. 17(b), where a lower stress level (50%) is applied, there is almost no crack observed in the model until the number of loading cycle reaches 96% of fatigue life. It must be emphasized that the crack initiation actually happens at the beginning of fatigue loading. However,

these cracks are at much smaller scales and cannot be detected in the model due to the limited resolution (5 μm). Therefore, there cracks manifest themselves as strength and stiffness reductions in diffused lattice elements instead of being explicitly represented in the model. When the cracks are observed in the model, significant damage has already been accumulated in the system. In addition, it can also be seen that some initial cracks are impeded by the HD C-S-H at the bottom-left corner of the microstructure. With the increasing number of loading cycles, the fatigue crack tends to propagate following the edge of the HD C-S-H and UHC. This is because at the low stress level the fatigue damage evolution rates for two C-S-H phases are significantly different. The damage accumulates much faster in LD C-S-H phases, and consequently, most of them have already been damaged before the fatigue failure. It is also found that the number of completely damaged elements ($D = 1$) in this fatigue simulation is almost 1.62 times higher than that of static fracture simulation. Therefore, the different degrees of damage in the microstructure leads to the final fatigue fracture pattern, which is
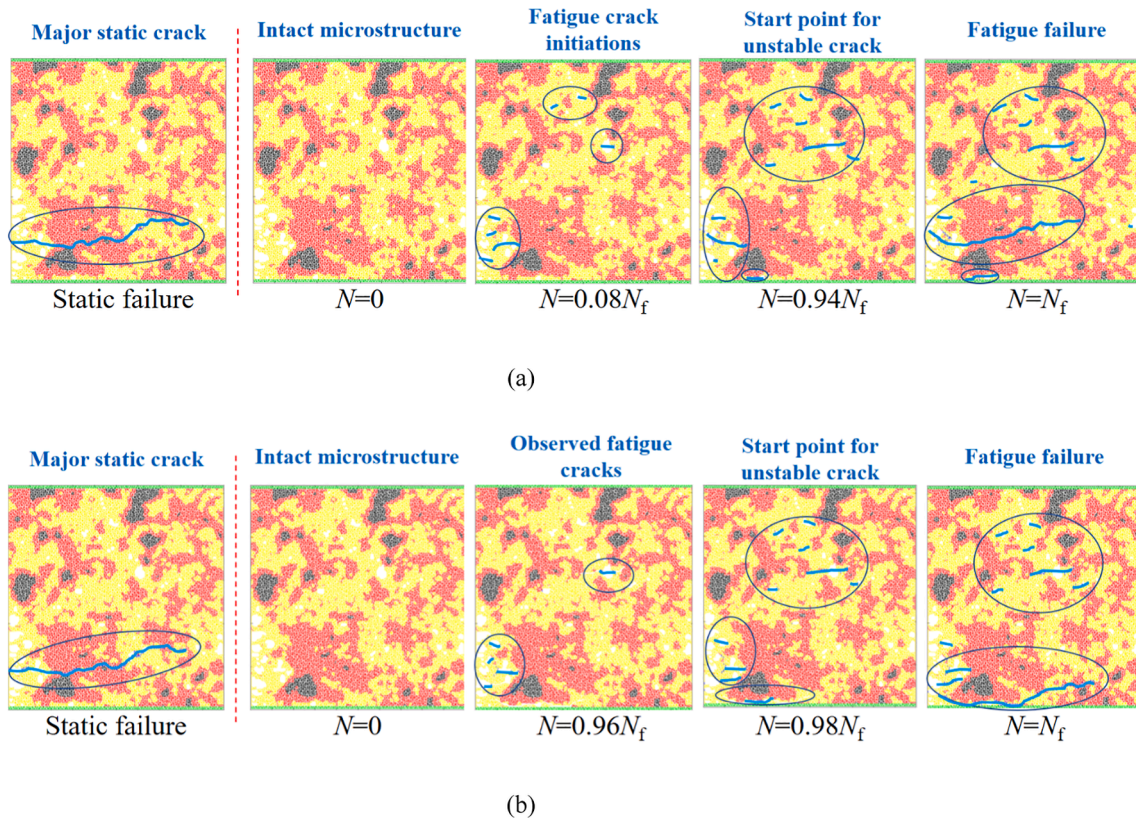

(a)

(b)

Fig. 17. Different fatigue fracture behaviours of cement pastes (w/c 0.4) under the (a) stress level of 85% (fatigue life $N_f = 3053$); and (b) the stress level of 50% (fatigue life $N_f = 3572216$).

different from the static fracture pattern.

Normally, the output of microscopic simulation results of cement pastes, e.g. *S-N* curves and fatigue damage evolutions, could be used as inputs for the macroscopic fatigue simulation of concrete. Similar to the static fracture multiscale modelling scheme [36,37], different fatigue properties should be assigned to different components in concrete. Since another major component of concrete, i.e. ITZ, is also crucial for its macroscopic fatigue behaviour, further researches on the microscopic fatigue behaviours of ITZ are needed.

5. Conclusions

In this study, a new 2D lattice fatigue model has been developed to investigate the fatigue behaviour of cement paste at the microscale. The experimental results for flexural fatigue of cement paste at the same length scale in author's previous work [40] are used to calibrate and validate the model.

In the current model the pre-peak fatigue damage evolution is introduced to local element based on the combined phenomenological *S-N* approach and Miner's law. The post-peak fatigue damage is considered using a cyclic constitutive law. Different fatigue damage evolution rates are assumed for various microscopic constituents of cement paste. In addition, the development of residual deformation can also be simulated by considering the creep and fatigue compliance of C-S-H phases. Overall, the proposed model can reproduce well the experimental results, in terms of *S-N* curve, stiffness degradation and residual deformation.

The validated model is then utilized to predict the uniaxial tensile fatigue fracture of cement paste. The effects of stress level and heterogeneity of the microstructure on the fatigue fracture pattern can be properly studied by the model. The major source of scatter for fatigue results originated from the heterogeneity of the microstructure can clearly be demonstrated by simulations. Combined with static fracture simulations, the simulations offer the opportunity to directly compare the static and fatigue fracture behaviours. It is found that the concurrent propagation of multiple cracks, other than a single crack in 2D static fracture simulation, is possible for the 2D fatigue simulation.

However, one major limitation of the current model is its 2D nature, which is unable to consider the 3D features of fatigue fracture behaviour in heterogeneous materials. Therefore, it is necessary to extend the current model to 3D simulations in a future study. Another limitation is the inherent empirical nature for the estimation of fatigue damage evolution, which lacks sufficient physical justifications. A clear physical explanation for the microscopic fatigue fracture may only exist on the atomic scale, where the propagation of the fatigue crack is assumed to be governed by the thermally activated breakage of atomic bonds [67]. Nevertheless, the current model has successfully demonstrated the effect of heterogeneity of the microstructure on the fatigue of cement paste in a very efficient way and provided some valuable insights into the microscopic fatigue fracture phenomenon. With the aid of the developed model, it is possible to predict the fatigue life of the cement paste for a given microstructure. Moreover, the output of simulation results at the microscale could potentially bring significant benefits for predicting the macroscopic fatigue of concrete in a multiscale framework.

Declaration of Competing Interest

The authors declare that they have no known competing financial interests or personal relationships that could have appeared to influence the work reported in this paper.

Acknowledgments

References

[1] Hsu TTC. Fatigue and microcracking of concrete. Matériaux Constr. 1984;17:51–4.

[2] Gao L, Hsu CTT. Fatigue of concrete under uniaxial compression cyclic loading. ACI Mater. J. 1998;95:575–81.

[3] Hsu TTC. Fatigue of Plain Concrete. ACI J. Proc. 1981;78:292–304.

[4] Keerthana K, Chandra Kishen JM. An experimental and analytical study on fatigue damage in concrete under variable amplitude loading. Int. J. Fatigue. 2018;111: 278–88.

[5] Kim JK, Kim YY. Experimental study of the fatigue behavior of high strength concrete. Cem. Concr. Res. 1996;26:1513–23.

[6] Li Q, Huang B, Xu S, Zhou B, Yu RC. Compressive fatigue damage and failure mechanism of fiber reinforced cementitious material with high ductility. Cem. Concr. Res. 2016;90:174–83.

[7] Gaedicke C, Roesler J, Shah S. Fatigue crack growth prediction in concrete slabs. Int. J. Fatigue. 2009;31:1309–17.

[8] Guo LP, Carpinteri A, Roncella R, Spagnoli A, Sun W, Vantadori S. Fatigue damage of high performance concrete through a 2D mesoscopic lattice model. Comput. Mater. Sci. 2009;44:1098–106.

[9] Mohammadipour A, Willam K. A numerical lattice method to characterize a contact fatigue crack growth and its Paris coefficients using configurational forces and stress-life curves. Comput. Methods Appl. Mech. Eng. 2018;340:236–52.

[10] Le JL, Manning J, Labuz JF. Scaling of fatigue crack growth in rock. Int. J. Rock Mech. Min. Sci. 2014;72:71–9.

[11] Bazant ZP, Hubler MH. Theory of cyclic creep of concrete based on Paris law for fatigue growth of subcritical microcracks. J. Mech. Phys. Solids. 2014;63:187–200.

[12] Bazant ZP, Xu K. Size effect in fatigue fracture of concrete. ACI Mater. J. 1991;88: 390–9.

[13] Carpinteri A, Spagnoli A. A fractal analysis of size effect on fatigue crack growth. Int. J. Fatigue. 2004;26:125–33.

[14] Carpinteri A, Spagnoli A, Vantadori S. A multifractal analysis of fatigue crack growth and its application to concrete. Eng. Fract. Mech. 2010;77:974–84.

[15] Hordijk D. Local approach to fatigue of concrete. Ph.D. Thesis. The Netherlands: Delft University of Technology, Delft; 1991.

[16] Hillerborg A, Modéer M, Petersson PE. Analysis of crack formation and crack growth in concrete by means of fracture mechanics and finite elements. Cem. Concr. Res. 1976;6:773–81.

[17] Mai SH, Le-corre F, Foret G, Nedjar B. A continuum damage modeling of quasi-static fatigue strength of plain concrete. Int. J. Fatigue. 2012;37:79–85.

[18] Zhaodong D, Jie L. A physically motivated model for fatigue damage of concrete. Int. J. Damage Mech. 2018;27:1192–212.

[19] Simon KM, Chandra Kishen JM. A multiscale approach for modeling fatigue crack growth in concrete. Int. J. Fatigue. 2017;98:1–13.

[20] Pichler C, Lackner R. Identification of logarithmic-type creep of calcium-silicate-hydrates by means of nanoindentation. Strain 2009;45:17–25.

[21] K. Van Breugel, Concrete: A material that barely deserves that qualification, in: Int. RILEM Conf. Mater. Sci., RILEM Publications SARL, 2010: pp. 13–32.

[22] Zhang H, Xu Y, Gan Y, Chang Z, Schlangen E, Šavija B. Microstructure informed micromechanical modelling of hydrated cement paste: Techniques and challenges. Constr. Build. Mater. 2020;251:118983.

[23] Gong F, Ueda T, Wang Y, Zhang D, Wang Z. Mesoscale simulation of fatigue behavior of concrete materials damaged by freeze-thaw cycles. Constr. Build. Mater. 2017;144:702–16.

[24] Corrado M, Molinari JF. Effects of residual stresses on the tensile fatigue behavior of concrete. Cem. Concr. Res. 2016;89:206–19.

[25] Guo LP, Carpinteri A, Spagnoli A, Sun W. Experimental and numerical investigations on fatigue damage propagation and life prediction of high-performance concrete containing reactive mineral admixtures. Int. J. Fatigue. 2010;32:227–37.

[26] Herrmann HJ, Roux S. Statistical models for the fracture of disordered media. Elsevier; 2014.

[27] Schlangen E, Garboczi EJ. Fracture simulations of concrete using lattice models: computational aspects. Eng. Fract. Mech. 1997;57:319–32.

[28] Schlangen E, van Mier JGM. Simple lattice model for numerical simulation of fracture of concrete materials and structures. Mater. Struct. 1992;25:534–42.

[29] Van Mier JGM. Concrete fracture: a multiscale approach. CRC Press; 2012.

[30] Man HK, Van Mier JGM. Damage distribution and size effect in numerical concrete from lattice analyses. Cem. Concr. Compos. 2011;33:867–80.

[31] Zhang H, Gan Y, Xu Y, Zhang S, Schlangen E, Šavija B. Experimentally informed fracture modelling of interfacial transition zone at micro-scale. Cem. Concr. Compos. 2019;104.

[32] Luković M, Šavija B, Schlangen E, Ye G, van Breugel K. A 3D lattice modelling study of drying shrinkage damage in concrete repair systems. Materials (Basel). 2016;9:9–13.

[33] Gan Y, Rodriguez CR, Zhang H. Modeling of microstructural effects on the creep of hardened cement paste using an experimentally informed lattice model. Comput. Civ. Infrastruct. Eng. 2021:1–17.

[34] Šavija B, Luković M, Schlangen E. Lattice modeling of rapid chloride migration in concrete. Cem. Concr. Res. 2014;61–62:49–63.

[35] Zhang H, Šavija B, Figueiredo SC, Lukovic M, Schlangen E. Microscale testing and modelling of cement paste as basis for multi-scale modelling. Materials (Basel). 2016;9.

[36] Zhang H, Šavija B, Luković M, Schlangen E. Experimentally informed micromechanical modelling of cement paste: An approach coupling X-ray computed tomography and statistical nanoindentation. Compos. Part B Eng. 2019; 157:109–22.

[37] Zhang H, Šavija B, Figueiredo SC, Schlangen E. Experimentally validated multi-scale modelling scheme of deformation and fracture of cement paste. Cem. Concr. Res. 2017;102:175–86.

[38] Zhang H, Šavija B, Xu Y, Schlangen E. Size effect on splitting strength of hardened cement paste: Experimental and numerical study. Cem. Concr. Compos. 2018;94: 264–76.

[39] Zhang H, Šavija B, Schlangen E. Combined experimental and numerical study on micro-cube indentation splitting test of cement paste. Eng. Fract. Mech. 2018;199: 773–86.

[40] Gan Y, Zhang H, Zhang Y, Xu Y, Schlangen E, van Breugel K, et al. Experimental study of flexural fatigue behaviour of cement paste at the microscale. Int. J. Fatigue. 2021;106378.

[41] Van Breugel K. Simulation of hydration and formation of structure in hardening cement-based materials. Ph.D. Thesis. The Netherlands: Delft University of Technology, Delft; 1991.

[42] Bishnoi S, Scrivener KL. μic: A new platform for modelling the hydration of cements. Cem. Concr. Res. 2009;39:266–74.

[43] Bentz DP. Modeling the influence of limestone filler on cement hydration using CEMHYD3D. Cem. Concr. Compos. 2006;28:124–9.

[44] Gan Y, Vandamme M, Zhang H, Chen Y, Schlangen E, van Breugel K, et al. Micro-cantilever testing on the short-term creep behaviour of cement paste at micro-scale. Cem. Concr. Res. 2020;134:1–26.

[45] Gan Y, Zhang H, Šavija B, Schlangen E, van Breugel K. Static and fatigue tests on cementitious cantilever beams using nanoindenter. Micromachines. 2018;9.

[46] Wong HS, Head MK, Buenfeld NR. Pore segmentation of cement-based materials from backscattered electron images. Cem. Concr. Res. 2006;36:1083–90.

[47] Tennis PD, Jennings HM. A model for two types of calcium silicate hydrate in the microstructure of Portland cement pastes. Cem. Concr. Res. 2000;30:855–63.

[48] Zhang H, Šavija B, Schlangen E. Towards understanding stochastic fracture performance of cement paste at micro length scale based on numerical simulation. Constr. Build. Mater. 2018;183:189–201.

[49] Yip M, Mohle J, Bolander JE. Automated modeling of three-dimensional structural components using irregular lattices. Comput. Civ. Infrastruct. Eng. 2005;20: 393–407.

[50] Qian Z. Multiscale modeling of fracture processes in cementitious materials. Ph.D. Thesis, Delft University of Technology, Delft, The Netherlands; 2012.

[51] Schlangen E. Experimental and numerical analysis of fracture process in concrete. Ph.D. Thesis. The Netherlands: Delft University of Technology, Delft; 1993.

[52] Zhang H, Xu Y, Gan Y, Chang Z, Schlangen E, Šavija B. Combined experimental and numerical study of uniaxial compression failure of hardened cement paste at micrometre length scale. Cem. Concr. Res. 2019;126.

[53] Lilliu G. 3D analysis of fracture processes in concrete. Ph.D. Thesis, Delft University of Technology, Delft, The Netherlands; 2007.

[54] Qiu J, Yang E. Micromechanics-based investigation of fatigue deterioration of engineered cementitious composite (ECC). Cem. Concr. Res. 2017;95:65–74.

[55] K. Nagai, Y. Sato, T. Ueda, Mesoscopic Simulation of Failure of Mortar and Concrete by 2D RBSM, 2 (2004) 359–374.

[56] E.W.C. Wilkins, Cumulative damage in fatigue, in: Colloq. Fatigue/Colloque Fatigue/Kolloquium Über Ermüdungsfestigkeit, Springer, 1956, pp. 321–332.

[57] Jan O, Holmen. Fatigue of Concrete by Constant and Variable Amplitude Loading. ACI Spec. Publ. 1982;75:71–110.

[58] Matsumoto K, Sato Y, Ueda T, Wang L. Mesoscopic analysis of mortar under high-stress creep and low-cycle fatigue loading. J. Adv. Concr. Technol. 2008;6:337–52.

[59] Schlitz W. A history of fatigue. Eng. Fract. Mech. 1996;54:263–300.

[60] Fathima KMP, Kishen JMC. A thermodynamic framework for the evolution of damage in concrete under fatigue. Arch. Appl. Mech. 2015;85:921–36.

[61] Sun B, Xu Z. An efficient numerical method for meso-scopic fatigue damage analysis of heterogeneous concrete. Constr. Build. Mater. 2021;278:122395.

[62] Reinhardt HW, Cornelissen HAW. Post-peak cyclic behaviour of concrete in uniaxial tensile and alternating tensile and compressive loading. Cem. Concr. Res. 1984;14:263–70.

[63] Gan Y, Rodriguez CR, Schlangen E, van Breugel K, Šavija B. Assessing strain rate sensitivity of cement paste at the micro-scale through micro-cantilever testing. Cem. Concr. Compos. 2021;121.

[64] Kirane K, Bažant ZP. Size effect in Paris law and fatigue lifetimes for quasibrittle materials: Modified theory, experiments and micro-modeling. Int. J. Fatigue. 2016; 83:209–20.

[65] R.R. Pedersen, A. Simone, M. Stroeven, L.J. Sluys, Mesoscopic modelling of concrete under impact, Proc. 6th Int. Conf. Fract. Mech. Concr. Concr. Struct. - Fract. Mech. Concr. Concr. Struct. 1 (2007) 571–578.

[66] Gan Y, Vandamme M, Chen Y, Schlangen E, van Breugel K, Šavija B. Experimental investigation of creep recovery of cement paste at the microscale. Cem Concr Res (submitted for publication).

[67] Le J-L, Bažant ZP. Unified nano-mechanics based probabilistic theory of quasibrittle and brittle structures: II. Fatigue crack growth, lifetime and scaling. J. Mech. Phys. Solids. 2011;59:1322–37.

[68] Toumi A, Bascoul A, Turatsinze A. Crack propagation in concrete subjected to flexural- cyclic loading. Mater. Struct. 1998;31:451–8.

[69] Simon KM, Kishen JMC. Influence of aggregate bridging on the fatigue behavior of concrete. Int. J. Fatigue. 2016;90:200–9.

[70] Saito M. Characteristics of microcracking in concrete under static and repeated tensile loading. Cem. Concr. Res. 1987;17:211–8.

[71] Zhang J, Li VC, Stang H. Size effect on fatigue in bending of concrete. J. Mater. Civ. Eng. 2001;13:446–53.